Chemical Engineering Journal 403 (2021) 126363

Contents lists available at ScienceDirect

Chemical Engineering Journal

journal homepage: www.elsevier.com/locate/cej

A direct Z-scheme oxygen vacant BWO/oxygen-enriched graphitic carbon nitride polymer heterojunction with enhanced photocatalytic activity

Xiuqin Huo[a,b,1], Yang Yang[a,b,1], Qiuya Niu[a,b,1], Yuan Zhu[a,b,1], Guangming Zeng[a,b,*], Cui Lai[a,b,*], Huan Yi[a,b], Minfang Li[a,b], Ziwen An[a,b], Danlian Huang[a,b], Yukui Fu[a,b], Bisheng Li[a,b], Ling Li[a,b], Mingming Zhang[a,b]

[a] *College of Environmental Science and Engineering, Hunan University, Changsha, Hunan 410082, China*
[b] *Key Laboratory of Environmental Biology and Pollution Control (Hunan University), Ministry of Education, Changsha, Hunan 410082, China*

HIGHLIGHTS

- A 3D BWO-OV/OCN heterojunction is prepared via facile hydrothermal process.
- The induced oxygen vacancies benefit the exposure of reaction sites.
- The black body nature of OCN enhances the light absorption capability.
- BWO-OV/OCN exhibits superior photocatalytic activity for efficient TC degradation.

ARTICLE INFO

Keywords:
OCN
BWO-OV
Oxygen vacancy
Z-scheme heterojunction photocatalyst
Tetracycline degradation

ABSTRACT

A high-performance micro-nano photocatalyst is urgently needed in the green and economical photocatalytic process for energy utilization and organic pollution control. Herein, a 3D Z-scheme heterojunction consisting of oxygen vacant bismuth tungstate nanosheets (BWO-OV) and oxygen-enriched graphitic carbon nitride (OCN) was developed, which shows large specific surface area and good electrical conductivity. A built-in electric field can be formed in this 3D structure, which accelerates the interfacial charge transfer. The oxygen vacancies of BWO-OV allow the formation of local defect energy levels below conduction band, which can improve the light harvesting capability. The oxygen-rich structure of OCN benefits the oxygen reduction to generate H_2O_2, and the black body nature enhance the light absorption capability. As expected, the BWO-OV/OCN heterojunction showed unusual photocatalytic efficiency toward the degradation of tetracycline (TC) (0.047 min^{-1}) under visible light. The photogenerated holes (h^+) and superoxide radicals ($\cdot O_2^-$) were found to play the main roles in TC degradation process. Moreover, the effect of actual water matrix on TC degradation over BWO-OV/OCN heterojunction was investigated. This work highlights a feasible way to design high-efficiency oxygen vacant bismuth-based photocatalysts, which shows the potential for real wastewater treatment.

1. Introduction

Recent years, water pollution caused by organic pollutants has become a serious problem [1–4]. More and more people have paid attention to the wastewater treatment [5–7]. Compared with the traditional technologies, such as adsorption process [8], ozone oxidation [9,10], electrochemical process [11,12] and biotreatment [13–15], photocatalysis, with broad application prospects in energy utilization and environmental pollution control [16–20], is a green and efficient method for organics removal from water [21–23].

Bismuth tungstate (BWO) with typical perovskite layered structure constructed by $[WO_4]^{2-}$ – $[Bi_2O_2]^{2+}$ – $[WO_4]^{2-}$ layers, has been developed for photocatalytic application under visible light irradiation. When electrons are photoexcited from Bi 4p orbital to Bi 6p orbital, the layered structure will form an internal electric field, which will help to enhance the separation of photogenerated carriers, and then improve the photocatalytic activity [24–26]. Inducing oxygen vacancy on BWO can tailor its electronic structures to allow the formation of local defect energy levels below conduction band (CB), which can improve the light harvesting capability [27]. Additionally, oxygen vacancies are the most

---

[*] Corresponding authors at: College of Environmental Science and Engineering, Hunan University, Changsha, Hunan 410082, China.
E-mail addresses: zgming@hnu.edu.cn (G. Zeng), laicui@hnu.edu.cn (C. Lai).

[1] These authors contribute equally to this article.

https://doi.org/10.1016/j.cej.2020.126363
Received 3 April 2020; Received in revised form 27 June 2020; Accepted 19 July 2020

reactive sites for reactants activation owing to the production of localized electrons [28].

Recently, oxygen vacant BWO (BWO-OV) with good photocatalytic activity, has attracted widespread attention. For example, Kong et al. [27] studied the photocatalytic activity of BWO-OV for CO_2 reduction. Yuan et al. [29] found that the introduced oxygen vacancy of BWO/$CuBi_2O_4$ Z-scheme heterojunction increased the generation of $\cdot O_2^-$, which benefited the tetracycline (TC) degradation. Wang et al. [30] designed $Bi_2WO_{6\text{-}x}$ nanosheets with tunable Bi quantum dots and oxygen vacancies, which exhibited the enhanced activity for selective oxidation of aromatic alcohols to carbonyl compounds in aqueous medium. Huo et al. [31] proved that BWO with gradient oxygen vacancies enhanced photocatalytic NO oxidation activity. Overall, BWO-OV shows great potential for photocatalysis. However, BWO-OV is limited by the carrier separation efficiency. Construct heterojunction is found to be an effective technology to solve this limitation [32,33].

Graphitized carbon nitride (g-C_3N_4), as a popular photocatalyst, shows large surface areas, fast carriers transport, and strong reduction ability of photogenerated electrons [34–36]. Constructing heterojunction with g-C_3N_4 is a mature way to enhance the photocatalytic activity [37–41]. Lately, Zhu's group [42] proposed a novel oxygen-enriched graphitic carbon nitride (OCN), which is synthesized by introducing C–O–C and –OH into the triazine ring structure of g-C_3N_4. The oxygen reducibility and carrier separation efficiency of OCN were proved to be better than g-C_3N_4. And OCN can generate H_2O_2 more easily owing to the oxygen-enriched structure and the black body nature enhance the light absorption capability [42]. The combination of OCN and BWO-OV was firstly proposed in this work to realize efficient separation efficiency and boost photocatalytic performance.

In this work, we constructed 3D BWO-OV/OCN heterojunction by simple hydrothermal method. The structure and morphology of prepared samples were explored via SEM and TEM. The photoelectric property was also studied in detail. The photocatalytic activity of samples was investigated via TC degradation. As an antibiotic, TC is widely used to treat bacterial infections in humans and livestock because of its high efficiency and wide spectrum [43,44]. But owing to its chemical stability and antibacterial nature, the released TC on water is hardly removed, and now being a threat for environment [45,46]. As a result, the removal of TC is urgent. Green and efficient methods are needed, like photocatalytic process in this work. The degradation intermediates of TC were analyzed through LC–MS, and then the decomposition pathway was discussed. Besides, the effects of actual water matrix and other reaction conditions on TC degradation over BWO-OV/OCN heterojunction were studied. The active radicals generated during the reaction were trapped by identified experiments to explore the role of dominating reactive radicals in the photodegradation process. For BWO-OV/OCN heterojunction, i) the induced oxygen vacancies benefit the exposure of reaction sites, ii) the black body nature and oxygen-rich structure of OCN would enhance the light absorption capability, and then the photocatalytic performance can be improved. Notably, this work provided a simple approach to synthesize high-efficiency oxygen vacant bismuth-based Z-scheme heterojunction photocatalyst, which is anticipated for the organics removal in real wastewater treatment.

2. Materials and methods

2.1. Materials

Octadecyltrimethylammonium chloride (OTAC) was brought from Shanghai Debai biotechnology Co. Ltd. Sodium tungstate dehydrate ($Na_2WO_4{\cdot}2H_2O$), Bismuth nitrate ($Bi(NO_3)_3{\cdot}5H_2O$), dicyandiamide ($C_2H_4N_4$), ammonium paratungstate ($H_{40}N_{10}O_{41}W_{12}{\cdot}xH_2O$), Tetracycline (TC), isopropanol (IPA), Tetramethylpiperidinyloxy (TEMPO) and sodium oxalate ($C_2Na_2O_4$) were purchased from sinopharm Chemical Reagent Co. Ltd.

2.2. Preparation of OCN

OCN was synthesized via simple calcination by previous report [42]. Firstly, 4.204 g (50 mmol) of dicyandiamide and 1.521 g (0.5 mmol) of ammonium paratungstate were transferred into a lidded corundum crucible to mix thoroughly. Then the mixture was calcined at 500 °C for 4 h with the heating rate of 3 °C min^{-1}. Finally, the product was obtained after cooling to room temperature.

2.3. Preparation of BWO-OV/OCN

0.1 g of $Na_2WO_4{\cdot}2H_2O$ (0.3 mmol) and 0.04 g of OTAC (0.115 mmol) were poured into 40 mL of deionized water. After completely dissolved, the powder of about 0.243 g of Bi $(NO_3)_3{\cdot}5H_2O$ (0.5 mmol) was added while being stirred on the multi-point magnetometer. After stirring for 1 h, 0.475 g the prepared OCN was added, and the new mixture was continued mixing overnight. The mixture was then transferred into teflon-lined high-pressure reactor (100 mL) and reacted in a 140 °C oven for 24 h. Finally, the obtained products after filtration were washed several times by deionized water and ethanol respectively. After drying at 60 °C for 12 h, the final 4BWO-OV/OCN composite was obtained. *x*BWO-OV/OCN (1: *x* in weight = OCN: BWO-OV in weight) heterojunction photocatalyst was obtained by adding different amount OCN. BWO-OV was prepared by the same procedure without adding OCN. The BWO-OV with different weight ratio in composite of 25 wt%, 50 wt%, 66 wt%, 75 wt%, 80 wt%, 83 wt% were prepared and signed as 0.33BWO-OV/OCN, 1BWO-OV/OCN, 2BWO-OV/OCN, 3BWO-OV/OCN, 4BWO-OV/OCN, 5BWO-OV/OCN, respectively.

2.4. Characterization

Powder X-ray diffraction (XRD-6100, Cu Kα radiation, λ = 0.15418 nm) was used to check the crystal structure of the prepared composites with the scanning range from 10° to 80°. Scanning electron microscopy (SEM) (SIGMA HD, Japan) was used to characterize the morphology and transmission electron microscope (TEM) (JEM-2010, JEOL, Japan) was used to check the crystal lattice parameters. The functional group of composites was collected on Fourier transform infrared spectrometer (NICOLET, iN10). And the specific surface areas and pore volume of the prepared composites were characterized by Brunauer-Emmett-Teller (BET) method. The surface chemical elemental compositions and valence state were examined using X-ray photoelectron spectroscopy (XPS, ESCALAB 250Xi spectrometer) with Al Kα source (hv = 1486.6 eV). The existence of oxygen vacancies was detected by electron paramagnetic resonance (EPR) analysis without light irradiation at the temperature of 77 K. Ultraviolet visible diffuse reflectance spectra (UV–vis DRS) were recorded on a Varian Cary 300 spectrophotometer from 200 to 800 nm ($BaSO_4$ as reference material).

2.5. Photocatalytic performance test

Under the irradiation of a 300 W Xe lamp (CEL-HXF300, Ceaulight) with 420 nm cut filter (155 mW cm^{-2}), TC degradation efficiency was used to evaluate the photocatalytic performances of the prepared composites. Before the irradiation, 0.1 L of TC solution (10 mg/L) with 0.02 g of OCN, BWO-OV, and *x*BWO-OV/OCN was stirred under the dark condition for 1 h to achieve adsorption saturation state. In the light experiment process, 0.003 L of the reaction solution was taken out at given time interval to filtrate with a 0.22 μm filter membrane. Then, the obtained TC solution was determined by a Shimadzu UV–vis spectrophotometer (UV-2770) with the characteristic peak at 357 nm. In the application of water matrix, the Xiangjiang River water, Taozi Lake water and tap water (Changsha, Hunan, China) were firstly filtrated by a 0.22 μm filter membrane and repeat the above steps. Finally, according to the analysis of the Liquid Chromatography-Mass (LC–MS) system, the degradation intermediates were detected. The detailed steps were presented in Supplementary material.

2.6. Photoelectrochemical and active species trapping experiments

Photoelectrochemical test was performed on electrochemical workstation (CHI760E). Sodium sulfate solution (Na_2SO_4, 0.2 M) was used as the electrolyte, and the light source was supplied by a 300 W xenon lamp (CEL-HXF300, Ceaulight) fitted with a 420 nm cutoff filter (155 mW cm^{-2}). The platinum wire was used as the counter electrode and Ag/AgCl electrode were utilized as the reference electrode. The working electrode was prepared by our photocatalyst: 0.01 g of the sample was appended to 0.001 L of 25% (W/V) PVA solution and sonicated for half an hour to get suspension. Then, the suspension was coated onto a fluorine-doped tinoxide (FTO) glass (1×2 cm^2) which was respectively precleaned by acetone, ethanol and deionized water. Finally, the obtained electrode was laid in an oven at 110 °C for 60 min. The photocurrent-time measurement (IT) was measured on an applied voltage of 0 V with the light on or off every 20 s. The electrochemical impedance spectroscopy (EIS) was collected on an applied voltage of 0 V with an amplitude of 0.005 V over a frequency between 10^{-2} and 10^5 Hz. Moreover, Mott-Schottky curve were also recorded at the frequency of 1000 Hz. The electron spin resonance (ESR) signals of radical were exhibited on a Bruker ER200-SRC spectrometer by engaging 5, 5-dimethyl-1-pyrroline N-oxide (DMPO) in water under visible light illumination. Moreover, sodium oxalate (SO-2Na), tetramethylpiperidine (TEMPO) and isopropyl alcohol (IPA) were used to further detected the effects of holes (h^+), superoxide radical ($\cdot O_2^-$) and hydroxyl ($\cdot OH$) on TC degradation.

3. Results and discussion

3.1. Characterizations

XRD was used to test the crystal structure of prepared materials. As shown in Fig. 1a, the XRD patterns of *x*BWO-OV/OCN heterojunction were overlapped the strong diffraction peaks of OCN and BWO-OV, which proved the two-phase composition. The peaks of BWO-OV located at 28.3°, 32.9°, 47.1°, 56.0°, 58.5°, 69.1°, 76.1° and 78.3° corresponded to the (1 3 1), (2 0 0), (2 0 2), (1 3 3), (2 6 2), (0 8 3), (2120) and (4 0 2) crystal planes of orthorhombic BWO (JCPDS NO. 39-0256), respectively [47]. There was no foreign peak, suggesting highly purified of the prepared samples. The peak of OCN at 27.46° was corresponding to the characteristic stacked conjugated aromatic systems peak (0 0 2) of g-C_3N_4 [48]. However, the peak of OCN in *x*BWO-OV/OCN heterojunction were uneasily to observe. This was probably because the intensity of diffraction peaks over OCN were much lower than BWO-OV. On the other hand, it was hard to differentiate the peak position of the (1 3 1) crystal plane of BWO-OV and (0 0 2) diffraction plane of OCN, which was quite close (28.41° *vs* 27.46°). In addition, the peak width of the (1 3 1) planes in composites (from 25.97° to 30.32°) was wider than BWO-OV (from 27.19° to 29.63°), that was might because the (0 0 2) diffraction plane of OCN was covered. According to the change of XRD pattern, it proved the successful preparation of composites.

The molecular structures of samples were further investigated by Fourier transform infrared (FTIR) spectra. Fig. 1b showed the relative FTIR spectra of OCN, BWO-OV and 4BWO-OV/OCN. The absorption bands of OCN at 3200 cm^{-1} and 800 cm^{-1} were related to the existence of O–H group [42] and the out-of-plane bending mode of the triazine units [49] respectively. And the stretching vibration of the C–O–C group was suggested by the absorption bands at 1273 and 1062 cm^{-1} [50,51]. As for BWO-OV, the obvious absorption bands at 3472 and 1622 cm^{-1} were owing to the stretching and bending of O–H group, respectively [52]. The obvious absorption bands at 581, 724 and 812 cm^{-1} were attributed to the stretching of Bi-O, W-O and W-O-W groups, respectively [52,53]. In addition, the absorption band at 1027 cm^{-1} was attributed to the stretching of C–O–C. The main absorption bands of BWO-OV were similar with the 4BWO-OV/OCN because BWO-OV was a carrier in the complex. Comparing with the spectrum of BWO-OV, the spectrum of 4BWO-OV/OCN changed at the range of 500–600 cm^{-1}, which attributed to the absorption of OCN.

The morphology and microstructure of OCN, BWO-OV and 4BWO-OV/OCN were characterized by SEM and HRTEM. SEM image in Fig. 2a presented the regular nanosheets of OCN. Fig. 2b showed that BWO-OV consisted of nanosheets with smooth surface. Fig. 2c showed that the microstructure of 4BWO-OV/OCN was similar to BWO-OV, but it was obvious that something covered on the surface of BWO-OV in SEM image of 4BWO-OV/OCN. These SEM images preliminarily proved the successful preparation of BWO-OV/OCN composite. More details were shown by HRTEM image. The HRTEM image of OCN were presented in Fig. S1. The d spacing value of the lattice fringe was 0.36 nm, corresponding to the OCN (0 0 2) plane. Fig. 2d showed the d spacing value of the lattice fringe was 0.273 nm, corresponding to the BWO-OV (2 0 0) plane [54]. The edge of prepared 4BWO-OV/OCN was square laminar in Fig. 2e. Fig. 2f verified the co-existence and intimate connection of OCN and BWO-OV. Except for the lattice fringe of BWO-OV, the d spacing values of the lattice fringe were 0.25 and 0.38 nm, which were respectively related to the (0 0 1) plane of graphite carbon and (0 0 2) plane of tungsten oxide [42]. The added tungsten source was conducive to the formation of oxygen-rich structures in OCN, but with the calcination temperature increasing, tungsten oxide was produced. The d spacing of 0.25 nm was slightly larger than g-C_3N_4 (0.24 nm) because of the information of oxygen-enriched structures. In addition, it was found a clear interface between OCN and BWO-OV. According to the above analysis, the BWO-OV/OCN heterojunction was formed, which was

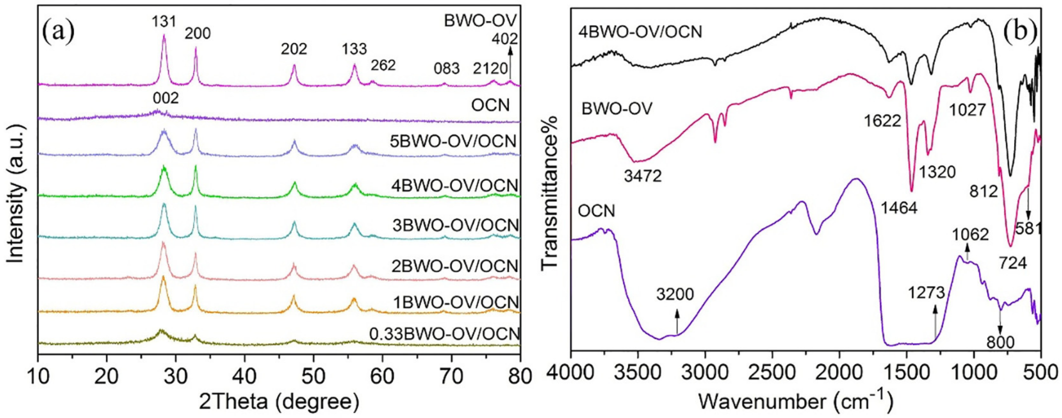

Fig. 1. (a) The XRD patterns of BWO-OV, OCN and *x*BWO-OV/OCN; (b) FT-IR spectra of OCN, BWO-OV and 4BWO-OV/OCN.

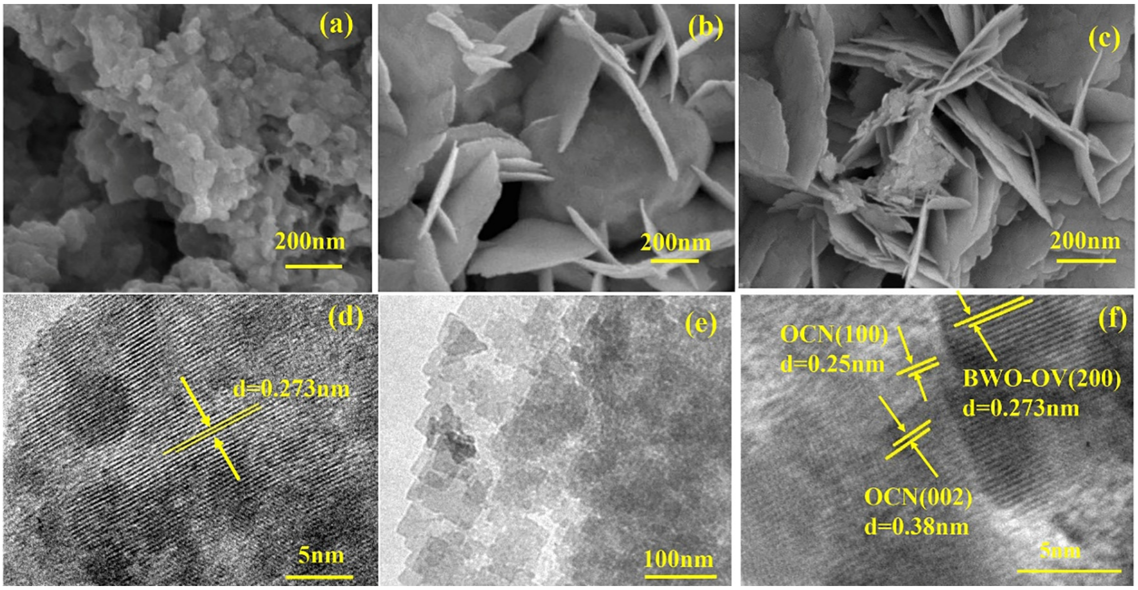

Fig. 2. SEM images of (a) OCN, (b) BWO-OV and (c) 4BWO-OV/OCN; TEM image of (d) BWO-OV, and (e and f) 4BWO-OV/OCN.

important in the following photocatalytic experiments to research their high photocatalytic performance.

The specific surface areas of OCN, BWO-OV and *x*BWO-OV/OCN were measured by N_2 adsorption-desorption isotherms. In Fig. 3a, the existence of mesopores were indicated by the typical IUPAC type IV pattern with a H_3 hysteresis pore based on the principles in the IUPAC Brunauer-Emmett-Teller classification [55,56]. According to Table S1, the specific surface areas of OCN, BWO-OV and 4BWO-OV/OCN were measured to be 35.98, 15.71 and 66.01 m^2/g, respectively. And the relative pore volumes were respectively 0.14, 0.09 and 0.35 cm^3/g. The surface area of 4BWO-OV/OCN was increased compared with OCN and BWO-OV because the presence of OCN enhanced the dispersion of BWO-OV [57]. The large surface area of composite could provide more reaction sites, which was similar with the adsorption performance.

The surface chemical elemental component and state were verified by XPS in Fig. 3b–f. Fig. 3b exhibited the XPS spectra of OCN, BWO-OV and 4BWO-OV/OCN, which suggested C and O were the primary elements. And the elements of BWO-OV and 4BWO-OV/OCN were nearly similar. The XPS spectra of C 1s (Fig. 3c) with three strong peaks at 288.0 and 286.1 eV were respectively assigned to the N=C–N and C–O, and the sp2 carbon was assigned to 284.8 eV [42]. However, around at 286.9 and 288.7 eV, two peaks related to C–O and COO bonds respectively showed up in BWO-OV and 4BWO-OV/OCN [58]. The O 1s XPS spectra (Fig. 3d) of OCN showed two strong peaks at 530.1 and 531.5 eV belonging to W-O and C-O, respectively. For the O 1s spectra (Fig. 3d) of 4BWO-OV/OCN and BWO-OV, three strong peaks around

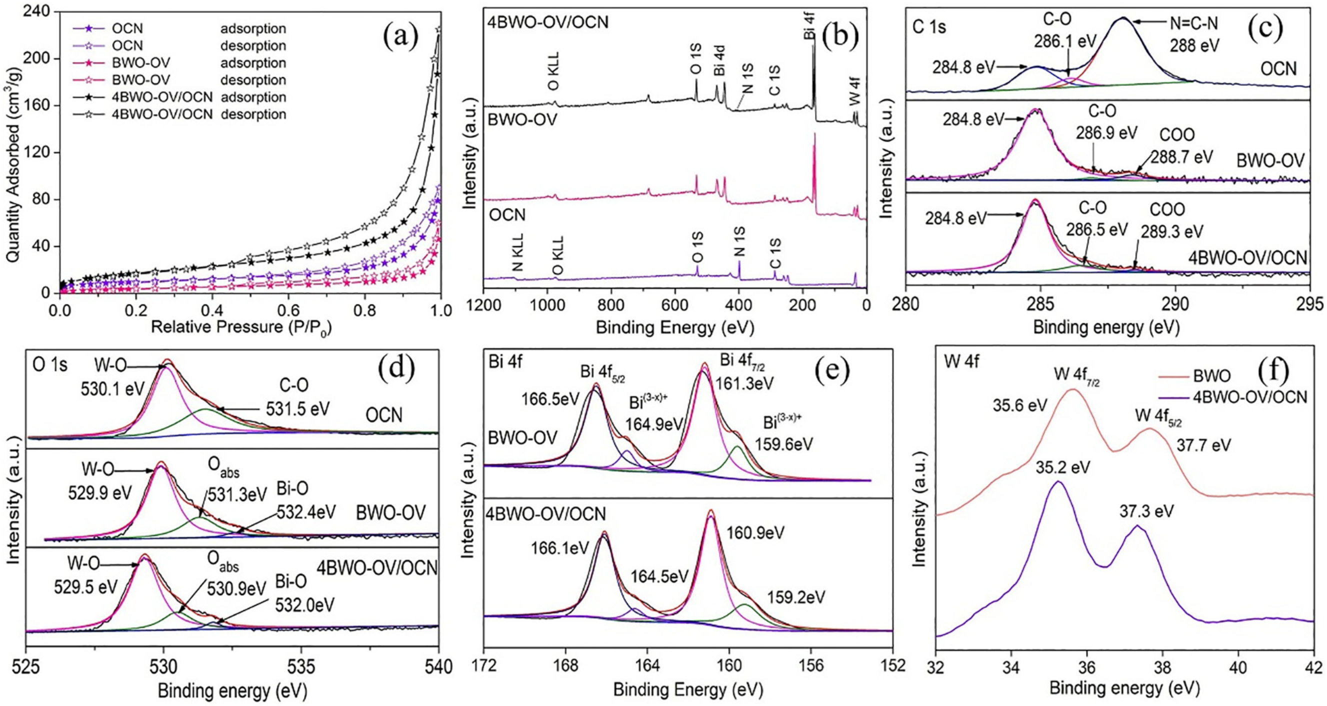

Fig. 3. (a) N_2 adsorption-desorption isotherms of OCN, BWO-OV and 4BWO-OV/OCN; XPS analysis of OCN, BWO-OV and *x*BWO-OV/OCN composite: (b) survey spectra, (c) C 1s, (d) O 1s; (e) Bi; (f) W 4f.

529.9, 531.3 and 532.4 eV belonged to W-O, surface chemisorbed oxygen species (O_{ads}) and Bi-O, respectively [30,59]. As expected, the peak intensity of surface chemisorbed oxygen species was strong, which reflected the concentration of oxygen vacancy [27]. The Bi 4f XPS spectra of BWO-OV and 4BWO-OV/OCN were showed in Fig. 3e. The binding energies of 166.1 and 160.9 eV (5.2 eV of doublet separation energy) in 4BWO-OV/OCN were belonging to Bi $4f_{7/2}$ and Bi $4f_{5/2}$ indicating the existence of Bi^{3+} [60]. In addition, there were two additional peaks at 159.2 and 164.5 eV, which came from Bi of lower valence state ($Bi^{(3-x)+}$) [61]. It might be related to the oxygen atoms loss within BWO-OV. Therefore, low-temperature solid-state electron paramagnetic resonance (EPR) was taken on to prove the existence of oxygen vacancy. The EPR signal of the oxygen vacancy could be seen in the Fig. S2. Therefore, the high-resolution Bi 4f XPS and EPR signal verified the existence of oxygen vacancy. Fig. 3f showed the W 4f XPS spectra of BWO-OV and 4BWO-OV/OCN, two main peaks of W 4f at 35.2 and 37.3 eV (2.1 eV of doublet separation energy) in 4BWO-OV/OCN belonged to W $4f_{7/2}$ and W $4f_{5/2}$, respectively. Compared with the O 1s, Bi 4f and W 4f XPS spectra of BWO-OV, the binding energy of 4BWO-OV/OCN shifted toward lower binding energies (~0.4 eV), which further proved the successful incorporation of OCN with BWO-OV.

3.2. Photoactivity test

In this work, the catalytic properties of *x*BWO-OV/OCN heterojunction were tested by the degradation efficiency of TC under irradiation. In addition, the effects of water source and other reaction conditions on the reaction results were also studied in detail. The adsorption of TC reached equilibrium after the dark reaction for 60 min. The absorbance spectra of TC were provided in Fig. S3, which suggested the TC degradation over 4BWO-OV/OCN. And the photocatalytic degradation efficiency of TC via *x*BWO-OV/OCN heterojunction was showed in Fig. 4. In Fig. 4a, 62.94% of TC was degraded by BWO-OV after 60 min irradiation. As for OCN, only 30.22% of TC was removed. The photocatalytic degradation efficiency of TC increased when the mass ratio of BWO-OV increased. TC removal efficiency reached highly 96.16% with mass ratio of BWO-OV increased to 80%. However, when the BWO-OV content was higher than 80%, the photocatalytic performance couldn't improve anymore. Besides, the photocatalytic degradation kinetics of TC was exhibited in Fig. 4b. 4BWO-OV/OCN was considered as the suitable photocatalyst to apply to the next photocatalytic tests because of its highest rate constant of 0.047 min^{-1}. And the comparison of the photocatalytic performance of 4BWO-OV/OCN and several reported catalysts was listed in Table S2.

Additionally, the degradation intermediates of TC were monitored through LC–MS method, which helped to put up the reaction mechanism. Table S3 exhibited the typical intermediates. In addition, Fig. S4 showed that as the reaction progressed, the intensity of the peak with *m/z* of 445 (TC) gradually decreased and almost disappeared after 60 min, which was similar with the photocatalytic degradation results. Holes (h^+) were vital for the degradation of TC, which caused N-demethylation process [62]. Hydroxyl (·OH) could cause dehydration and hydroxylation process, which also facilitated to the degradation of TC. The possible degradation processes were put forward in Fig. 5. There were three main degradation pathways. In the pathway I, TC was attacked by ·OH to produce intermediate NO2. Then NO2 was attacked by h^+ to generate NO3, which could participate in the pathway II. In the pathway II, h^+ could also directly attack NO1 to generate NO3, which could also be attacked via the N-demethylation to generate NO4. In the pathway III, because of the deamidation of TC, NO5 was produced, and then was converted to NO6 which was attributed to the shedding of dimethylamino. Due to the benzene rings opening and addition, shedding of hydroxyl and ethyl groups, NO7 and NO8 were detected. Finally, NO10 was generated through the abscission of acetyl group and oxidation reaction [63]. TC was degraded by suffering successive attacks. The degradation pathways were verified by previous studies [62,63]. In a word, these detected intermediates identified that 4BWO-OV/OCN made the progressive degradation of TC via the photocatalytic process.

Water matrix is vital on practical application. The effects of different water matrix on the degradation of TC by 4BWO-OV/OCN were researched via four different water matrixes, which were deionized water (DW), tap water (TW), Lake water (LW) and River water (RW). Fig. 6a showed the elaborate information of different water matrix. And Fig. 6b showed the photocatalytic degradation efficiency of TC attained 96.16%, 85.74%, 78.44%, and 84.80%, and the rate constant were 0.047 min^{-1}, 0.028 min^{-1}, 0.021 min^{-1}, and 0.028 min^{-1} (Fig. 6c) in UW, TW, LW, and RW, respectively. The Zeta potentials might well explain this phenomenon. If the Zeta potentials were more positive, the adsorption of TC on the catalysis could be inhibited. Adsorption is the first step of the reaction, which can affect the degradation efficiency of TC. The Zeta potentials of different water sources (Table 1) decreased in the order as follows: LW > RW > TW > DW, which was consistent with the degradation efficiency of TC.

In addition, electrolytes have strong effect on the photocatalytic activity. Therefore, it was significant to study the effect of different inorganic salt ions including NO_3^-, Cl^-, SO_4^{2-} and PO_4^{3-} on the practical application of photocatalytic technology. In Fig. 7a and b, all inorganic salt ions had an adverse impact on the photocatalytic degradation of TC, and the decreasing order was $PO_4^{3-} > SO_4^{2-} > Cl^- > NO_3^-$. It was reported that CO_3^{2-} not only could be used as hydroxyl radical quenchers but also competed adsorption sites with TC [63,64]. In addition, competition for the occupation of the active site led to the inhibition of SO_4^{2-} and NO_3^- [65]. All these reasons caused its negative effect on tetracycline

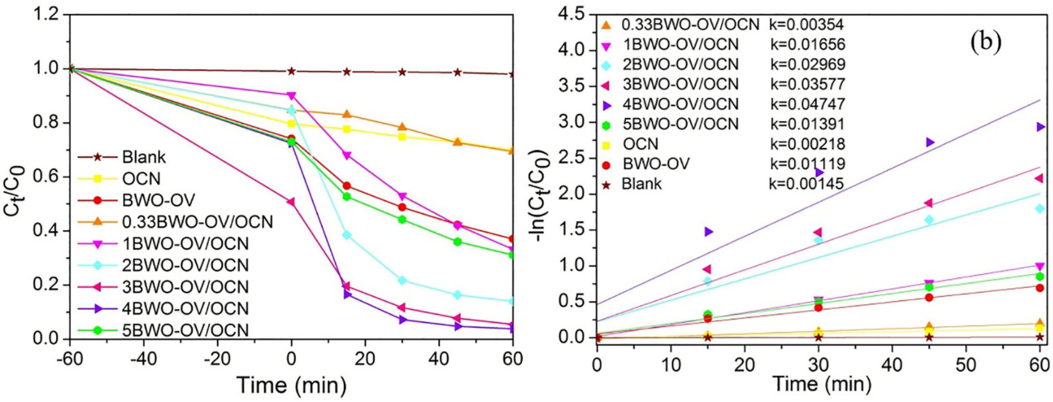

Fig. 4. (a) Degradation efficiency and (b) kinetics (k/min^{-1}) of TC under visible light by OCN, BWO-OV and *x*BWO-OV/OCN composites.

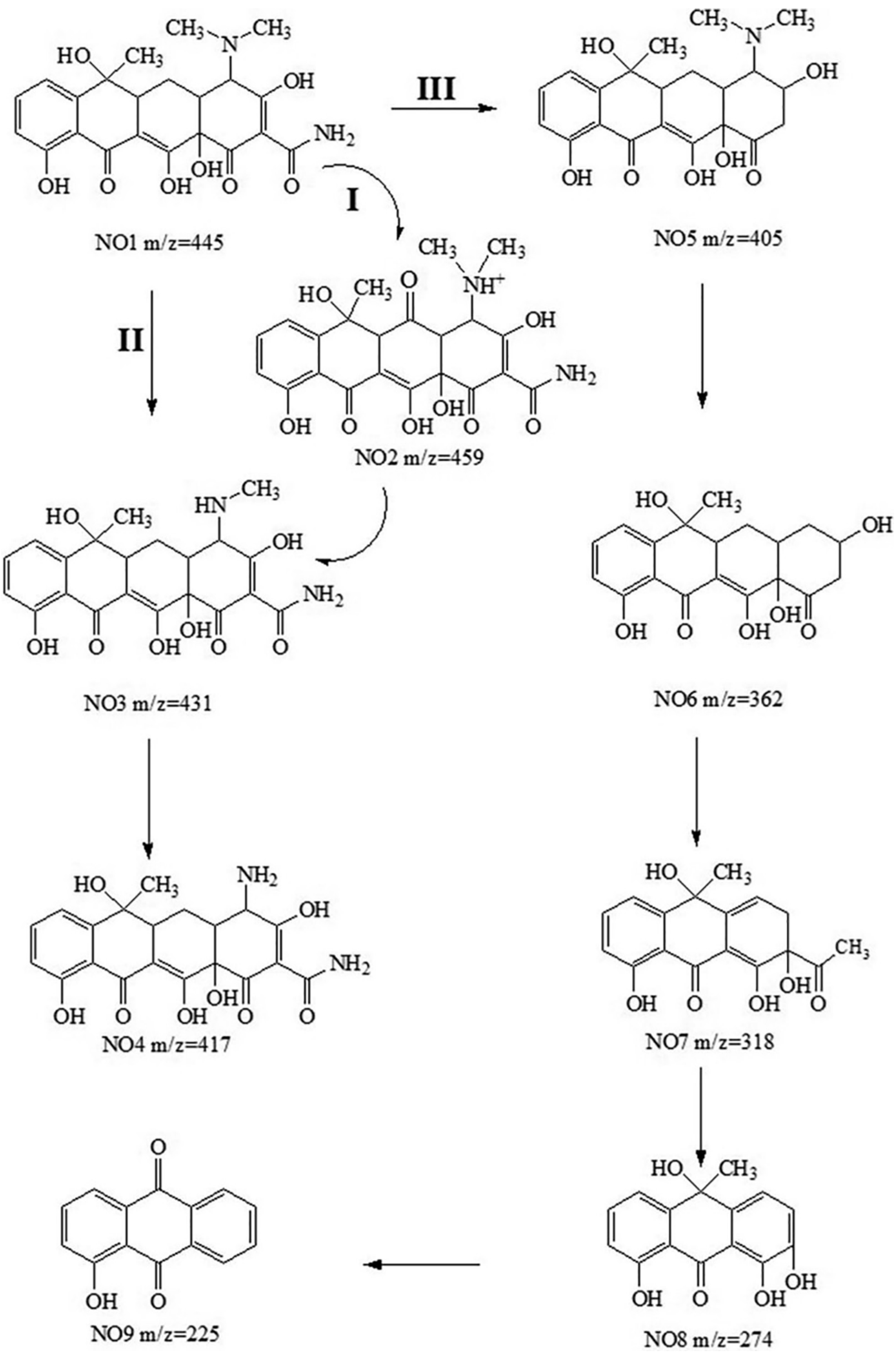

Fig. 5. The possible degradation processes of TC by 4BWO-OV/OCN under visible light irradiation.

degradation. Besides, the Zeta potentials could also explain the phenomenon [66]. Table 2 showed the Zeta potentials on TC solution, except for NO_3^-, the Zeta potentials of other ions were more positive than that of the condition (-2.46 ± 2.5), which might restrain the adsorption of TC on the catalysts. Hence, the enhanced electrostatic repulsion might decrease the photocatalytic efficiency and the competitive adsorption for the finite active sites were also reduced the photocatalytic efficiency [60]. As for NO_3^-, the main reason was that NO_3^- absorbed the solar light ranging from 290 to 370 nm, which caused the light-filtering effects. Hence, it had a certain negative effect on the photocatalytic reaction [67]. According to the above analysis, in practical application, the photocatalytic process by 4BWO-OV/OCN composite was an efficient technology.

3.3. Photocatalytic mechanism

3.3.1. Optical and electrical property

UV–vis DRS was used to verify the optical property of composites. Fig. 8a showed the UV–vis DRS spectra of OCN, BWO-OV and *x*BWO-OV/OCN, which could be found that the response edge of BWO-OV was shorter than 450 nm, while *x*BWO-OV/OCN showed enhanced the light absorption ability in the range of 450–800 nm. As a blackbody nature, OCN showed the highest light absorption. With the introduction of OCN, *x*BWO-OV/OCN had more efficient light utilization ability, which suggested OCN played an important role in the enhanced absorption of the visible light. Fig. 8b and c showed that the bandgap of OCN and BWO-OV were 2.51 and 2. 91 eV, which were obtained by the following

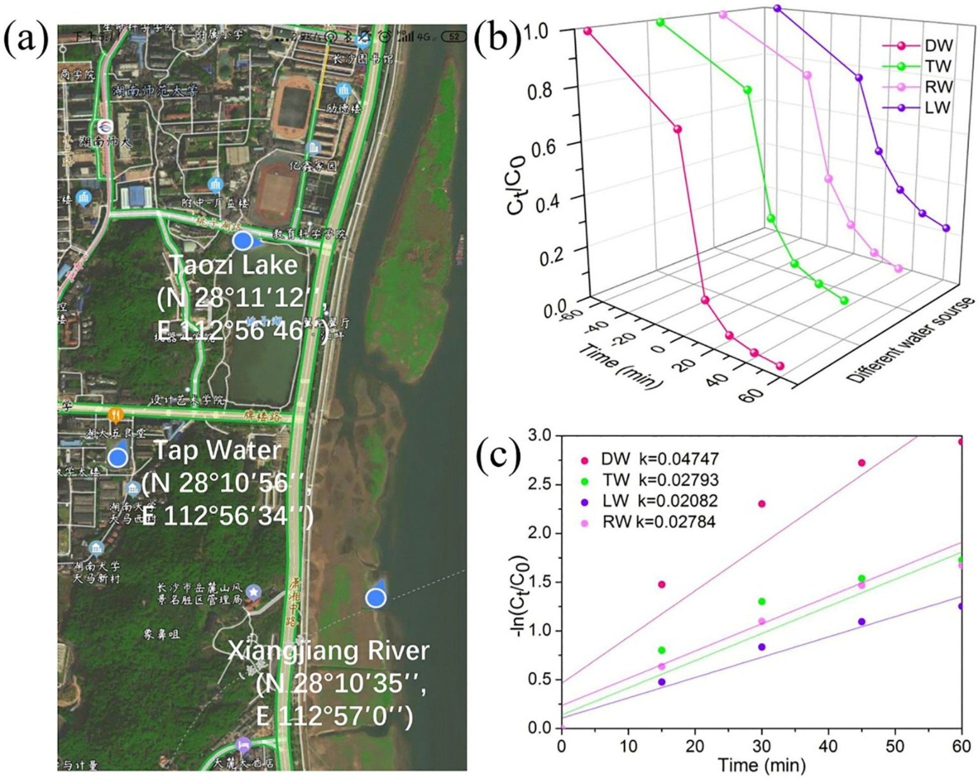

Fig. 6. (a) The elaborate information of different water sources; (b) degradation efficiency and (c) kinetics of TC by 4BWO-OV/OCN by using various water sources (k/min^{-1}).

Table 1
Zeta potentials and pH on different water sources containing 4BWO-OV/OCN.

Samples	DW	TW	RW	LW
Zeta potential (mV)	−2.46 ± 1.5	0.13 ± 2.0	41 ± 2.7	0.98 ± 2.3
pH	6.96	7.1	6.98	7.15

formula with the UV–vis DRS data:

$$\alpha hv = A\,(hv - E_g)^{n/2} \tag{1}$$

where α indicates the absorption coefficient, h indicates Planck constant, v indicates the light frequency, A indicates proportionality constant and E_g indicates the band gap energy. There are two value of n as 1 and 4. 1 is in keeping with direct band semiconductors, as for indirect band semiconductors, the value of n is 4. Therefore, the value of n for OCN and BWO-OV is 4.

$$E_{CB} = E_{VB} - E_g \tag{2}$$

where E_{CB} is conduction band, E_{vB} is valence band and E_g is the band gap. Fig. 8e and f showed the E_{VB} of OCN and BWO-OV were 1.93 and 2.59 eV, which were obtained from XPS spectra. Therefore, the E_{CB} of OCN and BWO-OV were assumed to be −0.60 and −0.32 eV.

We also proved this assumption by the Mott-Schottky experiment [60]. In Fig. 8h and i, the plot of OCN and BWO-OV were positive, indicating both of them were *n*-type semiconductor [68]. The results were also fitted with the previous reports that the flat band potential equaled the conduction band potential for n-type semiconductor [69]. The flat band potential was attained by extrapolating to the intercept of the x-axis. Therefore, the E_{CB} of OCN and BWO-OV could be speculated to be around −0.6 eV *vs.* NHE and −0.32 eV *vs.* NHE, which were fit with the deduction between UV–vis DRS and XPS spectra.

In addition, photoelectrochemical characteristics were also investigated by electrochemical impedance spectroscopy (EIS) and including photocurrent-time measurement (IT), which displayed the

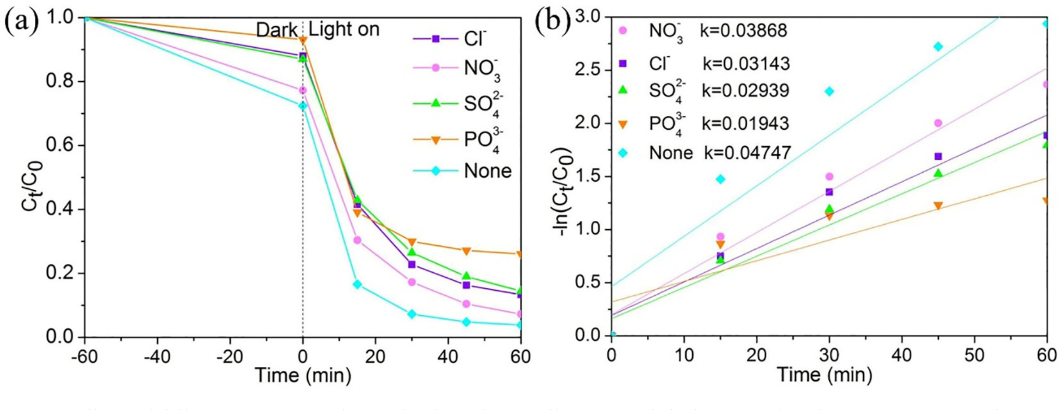

Fig. 7. (a) Effects of different inorganic salts on the degradation efficiency and (b) kinetics of TC by 4BWO-OV/OCN (k/min^{-1}).

Table 2
Zeta potentials and pH on the TC solution containing 4BWO-OV/OCN with different inorganic salt ions.

Inorganic salt ions	None	Na_3PO_4	Na_2SO_4	NaCl	Na_2NO_3
Zeta potential (mV)	−2.46 ± 1.5	1.9 ± 2.3	−0.49 ± 1.7	2.2 ± 3.3	−2.7 ± 1.9
pH	6.96	9.96	6.26	6.88	6.41

a. Test conditions: m/v = 0.2 g/L, TC (100 mL, 10 mg/L), and inorganic salt ions concentration (0.5 mM).

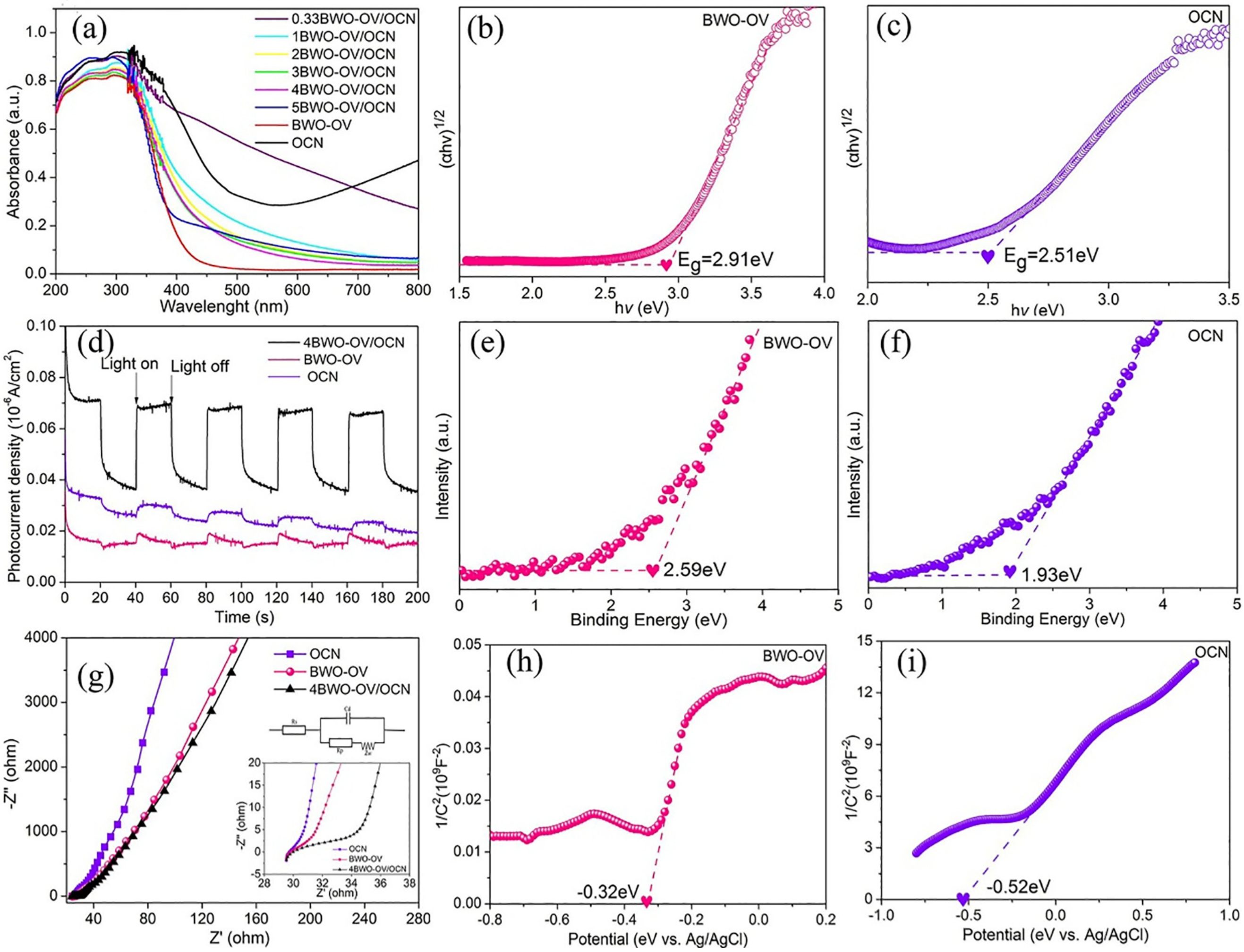

Fig. 8. UV–Vis diffuse reflectance of the prepared composites (a), the band gap energy of OCN (b) and BWO-OV (c), transient photocurrent response curves (d), the VB XPS spectra of OCN (e), and BWO-OV (f), EIS spectra (g), M-S analysis of OCN (h) and BWO-OV (i) film electrode in 0.5 M of Na_2SO_4 solution with pH set up in 5.96.

photoresponse ability and the transfer properties. In Fig. 8d, these samples, OCN, BWO-OV and 4BWO-OV/OCN exhibited obvious transient photocurrent response. 4BWO-OV/OCN showed higher photocurrent intensity under visible light irradiation, which proved the improved separation of electrons and holes. The results revealed 4BWO-OV/OCN exhibited the highest photocurrent response ability. The interfacial charge-carrier separation and transfer efficiencies were vindicated by EIS analysis. The EIS spectra of OCN, BWO-OV and 4BWO-OV/OCN were presented in Fig. 8g. Corresponding equivalent circuit diagram was inserted in Fig. 8g, which could be used to simulate the semicircles in the EIS Nyquist plots. 4BWO-OV/OCN shows a smaller semicircle radius and lower interfacial charge transfer resistance than OCN and BWO-OV, indicating the improvement of interfacial charge-carrier separation and transfer [70].

3.3.2. Roles of radical species

Radical species play important part in the photocatalytic degradation of most pollutants. The main radical species on the degradation process of TC by *x*BWO-OV/OCN were studied by ESR. Fig. 9a showed there was no ·OH radical signal. However, Video. S1 exhibited the composites generated a little ·OH radical in the first 15 s. It was suggested that ·OH radical was consumed fast, which proved ·OH radical didn't play important role in the reaction. Fig. 9b showed that $\cdot O_2^-$ radical signal was detected after visible light irradiation, proving the generation of $\cdot O_2^-$ radicals under irradiation. Hence, the photocatalytic performance of *x*BWO-OV/OCN heterojunction might improve. Active species trapping tests also were used for monitoring the radical species produced in the reaction. When SO-2Na, TEMPOL and IPA were added, the photocatalytic efficiency of TC degradation was different in Fig. 9c. It was clearly that SO-2Na and TEMPOL made the degradation efficiency restrain greatly, while IPA made it decrease

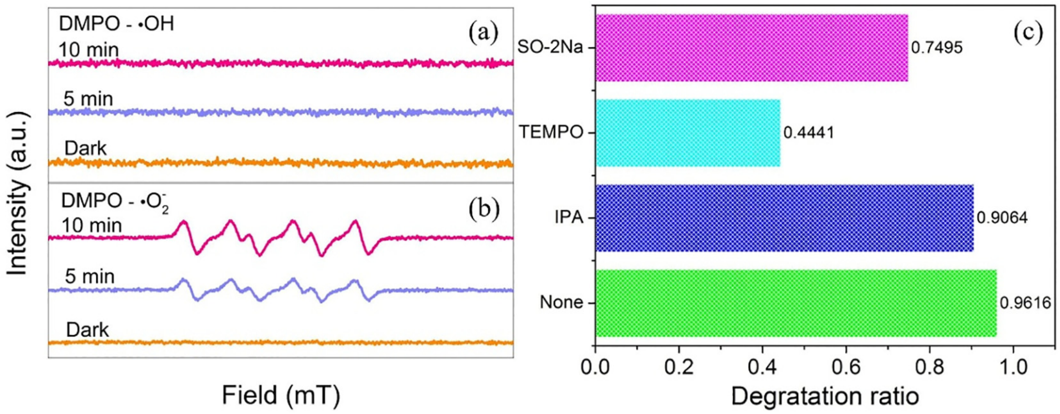

Fig. 9. DMPO spin-trapping ESR spectra of 4BWO-OV/OCN composites: (a) in aqueous dispersion for DMPO-$\cdot OH$ and (b) in aqueous dispersion for DMPO-$\cdot O_2^-$; (c) scavenger tests: 5 mmol scavengers of TEMPO, 10 mmol of SO-2Na and IPA in 100 mL 10 mg/L TC solution.

slightly, indicating that h^+ and $\cdot O_2^-$ were vital to the catalytic reaction. As for $\cdot OH$ radicals, just a little amount of them took part in photocatalytic degradation of TC.

3.3.3. *Possible mechanism of the enhanced photocatalytic activity*

According to the above analysis, a possible Z-scheme mechanism for degradation of tetracycline was proposed in Fig. 10. The VB of composites was 2.53 eV, close to that of BWO-OV, which meant the h^+ still on the BWO-OV in 4BWO-OV/OCN. According to the previous reports, it might form direct Z-scheme [71]. In addition, based on the analysis of radical species, the $\cdot O_2^-$ and $\cdot OH$ species were also taken part in the reaction, which meant the generation of the species. Because the CB of BWO-OV (−0.32 eV) was more positive than that of $O_2/\cdot O_2^-$ (−0.33 eV), and the VB of OCN (1.93 eV) was more negative than that of $H_2O/\cdot OH$ (2.4 eV) [60], according to the traditional heterojunction transfer process, there were no production of $\cdot O_2^-$ and $\cdot OH$ species. Hence, it was reasonable to propose Z-scheme mechanism. In all, the reaction could be summarized as follows: OCN and BWO-OV generated electrons and holes under visible light irradiation. And the photogenerated electrons of BWO-OV would recombine with the holes of OCN, which could form a built-in electric field to accelerate the interfacial charge transfer and separation. The left excited electrons and holes possessed higher reduction and oxidation capability. The dissolved O_2 could be restored to $\cdot O_2^-$ by the electrons of OCN, which would be used for TC degradation. And according to previous reported, the existence of tungsten oxide in OCN accelerated the oxidation of H_2O_2 generated by OCN to O_2. Therefore, there were more oxygen in the solution to make $\cdot O_2^-$ radicals. The holes of BWO-OV could directly oxidize TC. In addition, the holes also reacted with H_2O to generate $\cdot OH$. But because of the low number of $\cdot OH$ radicals, they were consumed before they could participate in the reaction.

3.3.4. *Stability of synthesized catalyst*

The stability and recyclability of 4BWO-OV/OCN were also investigated in TC photodegradation. Fig. 11a showed the results of the cyclic experiments over 4BWO-OV/OCN which was reused in four reaction runs. Obviously, after four cycles, the TC photodegradation efficiency dropped to 81.1%, which also maintained high degradation efficiency for TC. It was clearly that after the first cyclic experiment, the adsorption performance decreased apparently. It might be due to a small amount of contamination on the surface of the composite, the active sites were blocked. In addition, the oxygen vacancies of BWO-OV might be consumed due to the instability of oxygen vacancies. However, the photocatalytic system reached stable in the following cycling

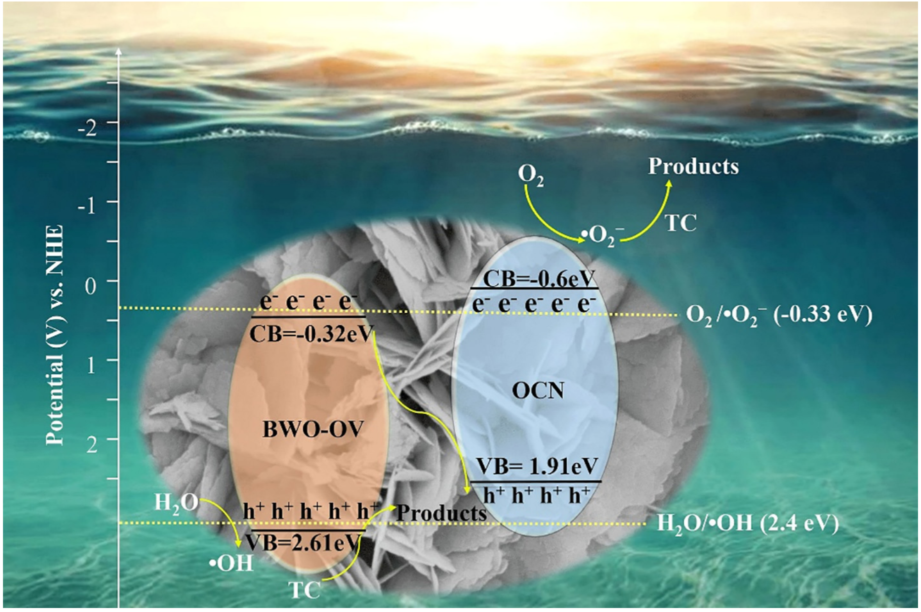

Fig. 10. Possible photocatalytic degradation mechanism scheme by 4BWO-OV/OCN under visible light irradiation.

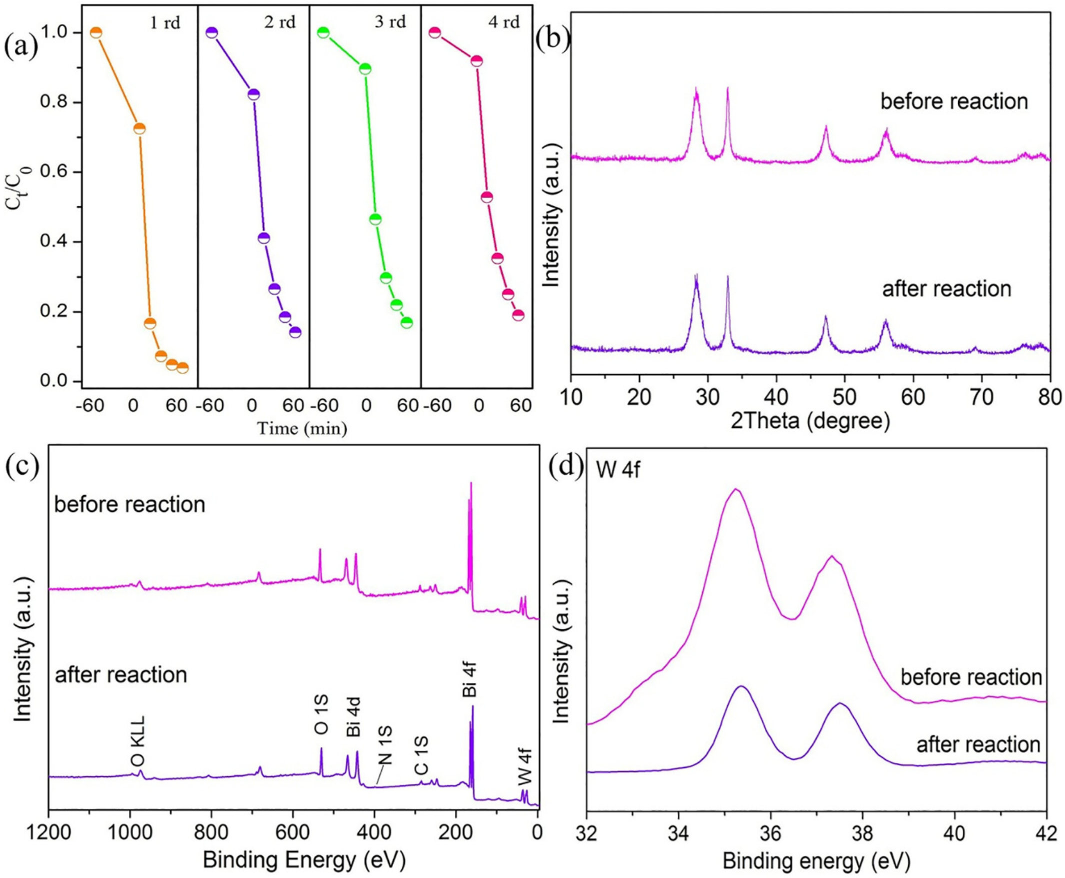

Fig. 11. (a) Cycling experiment of TC photodegradation by 4BWO-OV/OCN; (b) XRD analysis of fresh and Used 4BWO-OV/OCN; XPS analysis of fresh and Used 4BWO-OV/OCN: (c) survey spectra, (d) W 4f.

runs. In addition, the XRD of 4BWO-OV/OCN was measured after the photocatalytic reaction (Fig. 11b). It was confirmed the same crystal phases of fresh sample and used sample. Besides, Fig. 11(c-d) showed the XPS spectra of the fresh and used 4BWO-OV/OCN, including the survey spectra and W 4f. The elemental composites and valence state of 4BWO-OV/OCN stayed the same after the photodegradation reaction. The XPS spectra of C and O (Fig. S5) were mainly similar. The slightly difference in the XPS spectrum of C might be due to a small amount of contamination on the surface of the composite. In the XPS spectrum of O, the surface chemisorbed oxygen species was weakly, which might attribute to the instability of oxygen vacancies. The XPS spectrum of Bi 4f was also measured in Fig. S6. In comparison, the used sample shifted to lower binding energy, which was might attributed to the instability of oxygen vacancies. And the disappearance of $Bi^{(3-x)+}$ further confirmed the consumed of oxygen vacancies. Hence, how to improve the stability of oxygen vacancies posed a challenge for our future work. Moreover, SEM and FTIR of the used 4BWO-OV/OCN were tested to prove the stability in Figs. S7 and S8. It was found that there were no distinct changes. In general, the stability of 4BWO-OV/OCN composite was illustrated for the TC photodegradation.

4. Conclusion

In this work, 3D BWO-OV/OCN heterojunction was successfully prepared via facile hydrothermal process. The successful recombination of heterojunction was demonstrated by SEM, TEM and XPS analysis. The BWO-OV/OCN heterojunction exhibited several superiorities: i) the induced oxygen vacancies benefit the exposure of reaction sites, ii) the black body nature and oxygen-rich structure of OCN would enhance the light absorption capability, and then the photocatalytic performance can be improved. 4BWO-OV/OCN heterojunction exhibited the best performance which enabled TC (10 mg/L) removal rate to reach 96.16% within 60 min, more than double that of pristine OCN (30.22%) and higher than that of pure BWO-OV (62.94%) under the same conditions. h^+ and $\cdot O_2^-$ were vital to the TC photocatalytic degradation by ESR analysis and scavenger tests. The synthesized 4BWO-OV/OCN also exhibited high degradation efficiencies towards TC in real water matrix, which provides a potential strategy to develop photocatalysts for pollutant elimination in practice.

Declaration of Competing Interest

The authors declare that they have no known competing financial interests or personal relationships that could have appeared to influence the work reported in this paper.

Acknowledgements

This study was financially supported by the Program for the National Natural Science Foundation of China (51521006, 51879101, 51579098, 51779090, 51909084), the National Program for Support of Top–Notch Young Professionals of China (2014), the Program for Changjiang Scholars and Innovative Research Team in University (IRT-13R17), the Fundamental Research Funds for the Central Universities (531119200086, 531118010114, 541109060031), the Hunan Provincial Innovation Foundation for Postgraduate (CX20190260) and the Three Gorges Follow-up Research Project (2017HXXY-05).

Appendix A. Supplementary data

Supplementary data to this article can be found online at https://doi.org/10.1016/j.cej.2020.126363.

References

[1] A. Serrà, Y. Zhang, B. Sepúlveda, E. Gómez, J. Nogués, J. Michler, L. Philippe, Highly reduced ecotoxicity of ZnO-based micro/nanostructures on aquatic biota: influence of architecture, chemical composition, fixation, and photocatalytic efficiency, Water Res. 169 (2020) 115210.

[2] S. Talwar, A.K. Verma, V.K. Sangal, U.L. Štangar, Once through continuous flow removal of metronidazole by dual effect of photo-Fenton and photocatalysis in a compound parabolic concentrator at pilot plant scale, Chem. Eng. J. 388 (2020) 124184.

[3] L. Li, C. Lai, F. Huang, M. Cheng, G. Zeng, D. Huang, B. Li, S. Liu, M. Zhang, L. Qin, M. Li, J. He, Y. Zhang, L. Chen, Degradation of naphthalene with magnetic bio-char activate hydrogen peroxide: synergism of bio-char and Fe-Mn binary oxides, Water Res. 160 (2019) 238–248.

[4] S.R. Patil, B.H. Hameed, A.S. Škapin, U.L. Štangar, Alternate coating and porosity as dependent factors for the photocatalytic activity of sol–gel derived TiO2 films, Chem. Eng. J. 174 (2011) 190–198.

[5] B. Song, Z. Zeng, G. Zeng, J. Gong, R. Xiao, S. Ye, M. Chen, C. Lai, P. Xu, X. Tang, Powerful combination of g-C3N4 and LDHs for enhanced photocatalytic performance: a review of strategy, synthesis, and applications, Adv. Colloid Interface Sci. 272 (2019).

[6] C. Zhou, Z. Zeng, G. Zeng, D. Huang, R. Xiao, M. Cheng, C. Zhang, W. Xiong, C. Lai, Y. Yang, W. Wang, H. Yi, B. Li, Visible-light-driven photocatalytic degradation of sulfamethazine by surface engineering of carbon nitride: properties, degradation pathway and mechanisms, J. Hazard. Mater. 380 (2019) 120815–120815.

[7] J. Cai, J. Huang, S. Wang, J. Iocozzia, Z. Sun, J. Sun, Y. Yang, Y. Lai, Z. Lin, Crafting mussel-inspired metal nanoparticle-decorated ultrathin graphitic carbon nitride for the degradation of chemical pollutants and production of chemical resources, Adv. Mater. 31 (2019) 1806314.

[8] J.L. Gong, B. Wang, G.M. Zeng, C.P. Yang, C.G. Niu, Q.Y. Niu, W.J. Zhou, Y. Liang, Removal of cationic dyes from aqueous solution using magnetic multi-wall carbon nanotube nanocomposite as adsorbent, J. Hazard. Mater. 164 (2009) 1517–1522.

[9] L. Bilinska, K. Blus, M. Gmurek, S. Ledakowicz, Coupling of electrocoagulation and ozone treatment for textile wastewater reuse, Chem. Eng. J. 358 (2019) 992–1001.

[10] F.J. Rivas, R.R. Solís, F.J. Beltrán, O. Gimeno, Sunlight driven photolytic ozonation as an advanced oxidation process in the oxidation of bezafibrate, cotinine and iopamidol, Water Res. 151 (2019) 226–242.

[11] C. Lai, S. Liu, C. Zhang, G. Zeng, D. Huang, L. Qin, X. Liu, H. Yi, R. Wang, F. Huang, B. Li, T. Hu, Electrochemical aptasensor based on sulfur nitrogen codoped ordered mesoporous carbon and thymine-Hg2+-thynnine mismatch structure for Hg2+ detection, ACS Sens. 3 (2018) 2566–2573.

[12] N. Mameda, H. Park, K.-H. Choo, Electrochemical filtration process for simultaneous removal of refractory organic and particulate contaminants from wastewater effluents, Water Res. 144 (2018) 699–708.

[13] Y. Wang, Y. Zhu, Y. Hu, G. Zeng, Y. Zhang, C. Zhang, C. Feng, How to construct DNA hydrogels for environmental applications: advanced water treatment and environmental analysis, Small 14 (2018).

[14] X. Tang, G. Zeng, C. Fan, M. Zhou, L. Tang, J. Zhu, J. Wan, D. Huang, M. Chen, P. Xu, C. Zhang, Y. Lu, W. Xiong, Chromosomal expression of CadR on Pseudomonas aeruginosa for the removal of Cd(II) from aqueous solutions, Sci. Total Environ. 636 (2018) 1355–1361.

[15] S. Ye, G. Zeng, H. Wu, C. Zhang, J. Dai, J. Liang, J. Yu, X. Ren, H. Yi, M. Cheng, C. Zhang, Biological technologies for the remediation of co-contaminated soil, Crit. Rev. Biotechnol. 37 (2017) 1062–1076.

[16] P. Xu, G.M. Zeng, D.L. Huang, C.L. Feng, S. Hu, M.H. Zhao, C. Lai, Z. Wei, C. Huang, G.X. Xie, Z.F. Liu, Use of iron oxide nanomaterials in wastewater treatment: a review, Sci. Total Environ. 424 (2012) 1–10.

[17] H. Wang, Z.T. Zeng, P. Xu, L.S. Li, G.M. Zeng, R. Xiao, Z.Y. Tang, D.L. Huang, L. Tang, C. Lai, D.N. Jiang, Y. Liu, H. Yi, L. Qin, S.J. Ye, X.Y. Ren, W.W. Tang, Recent progress in covalent organic framework thin films: fabrications, applications and perspectives, Chem. Soc. Rev. 48 (2019) 488–516.

[18] C. Xu, P. Ravi Anusuyadevi, C. Aymonier, R. Luque, S. Marre, Nanostructured materials for photocatalysis, Chem. Soc. Rev. 48 (2019) 3868–3902.

[19] D. Jiang, M. Chen, H. Wang, G. Zeng, D. Huang, M. Cheng, Y. Liu, W. Xue, Z. Wang, The application of different typological and structural MOFs-based materials for the dyes adsorption, Coord. Chem. Rev. 380 (2019) 471–483.

[20] C. Lai, X. Liu, L. Qin, C. Zhang, G. Zeng, D. Huang, M. Cheng, P. Xu, H. Yi, D. Huang, Chitosan-wrapped gold nanoparticles for hydrogen-bonding recognition and colorimetric determination of the antibiotic kanamycin, Microchim. Acta 184 (2017) 2097–2105.

[21] X. Meng, L. Liu, S. Ouyang, H. Xu, D. Wang, N. Zhao, J. Ye, Nanometals for solar-to-chemical energy conversion: from semiconductor-based photocatalysis to plasmon-mediated photocatalysis and photo-thermocatalysis, Adv. Mater. 28 (2016) 6781–6803.

[22] X. Zhou, C. Lai, D. Huang, G. Zeng, L. Chen, L. Qin, P. Xu, M. Cheng, C. Huang, C. Zhang, C. Zhou, Preparation of water-compatible molecularly imprinted thiol-functionalized activated titanium dioxide: selective adsorption and efficient photodegradation of 2, 4-dinitrophenol in aqueous solution, J. Hazard. Mater. 346 (2018) 113–123.

[23] S.C. Pillai, U.L. Štangar, J.A. Byrne, A. Pérez-Larios, D.D. Dionysiou, Photocatalysis for disinfection and removal of contaminants of emerging concern, Chem. Eng. J. 261 (2015) 1–2.

[24] B. Li, C. Lai, G. Zeng, L. Qin, H. Yi, D. Huang, C. Zhou, X. Liu, M. Cheng, P. Xu, C. Zhang, F. Huang, S. Liu, Facile hydrothermal synthesis of Z-scheme $Bi_2Fe_4O_9$/Bi_2WO_6 heterojunction photocatalyst with enhanced visible-light photocatalytic activity, ACS Appl. Mater. Interfaces 10 (2018) 18824–18836.

[25] Y. Yang, C. Zhang, C. Lai, G. Zeng, D. Huang, M. Cheng, J. Wang, F. Chen, C. Zhou, W. Xiong, BiOX (X = Cl, Br, I) photocatalytic nanomaterials: applications for fuels and environmental management, Adv. Colloid Interface Sci. 254 (2018) 76–93.

[26] X. Lu, W. Che, X. Hu, Y. Wang, A. Zhang, F. Deng, S. Luo, D.D. Dionysiou, The facile fabrication of novel visible-light-driven Z-scheme $CuInS_2$/Bi_2WO_6 heterojunction with intimate interface contact by in situ hydrothermal growth strategy for extraordinary photocatalytic performance, Chem. Eng. J. 356 (2019) 819–829.

[27] X.Y. Kong, Y.Y. Choo, S.P. Chai, A.K. Soh, A.R. Mohamed, Oxygen vacancy induced Bi2WO6 for the realization of photocatalytic CO2 reduction over the full solar spectrum: from the UV to the NIR region, Chem. Commun. (Camb.) 52 (2016) 14242–14245.

[28] Y. Sun, H. Wang, Q. Xing, W. Cui, J. Li, S. Wu, L. Sun, The pivotal effects of oxygen vacancy on Bi2MoO6: promoted visible light photocatalytic activity and reaction mechanism, Chin. J. Catal. 40 (2019) 647–655.

[29] X. Yuan, D. Shen, Q. Zhang, H. Zou, Z. Liu, F. Peng, Z-scheme Bi2WO6/CuBi2O4 heterojunction mediated by interfacial electric field for efficient visible-light photocatalytic degradation of tetracycline, Chem. Eng. J. 369 (2019) 292–301.

[30] J. Wang, H. Liang, C. Zhang, B. Jin, Y. Men, Bi2WO6-x nanosheets with tunable Bi quantum dots and oxygen vacancies for photocatalytic selective oxidation of alcohols, Appl. Catal. B 256 (2019) 117874.

[31] W.C. Huo, X.a. Dong, J.Y. Li, M. Liu, X.Y. Liu, Y.X. Zhang, F. Dong, Synthesis of Bi2WO6 with gradient oxygen vacancies for highly photocatalytic NO oxidation and mechanism study, Chem. Eng. J. 361 (2019) 129–138.

[32] R. Wu, H. Song, N. Luo, G. Ji, Hydrothermal preparation of 3D flower-like BiPO4/Bi2WO6 microsphere with enhanced visible-light photocatalytic activity, J. Colloid Interface Sci. 524 (2018) 350–359.

[33] S. Ye, M. Yan, X. Tan, J. Liang, G. Zeng, H. Wu, B. Song, C. Zhou, Y. Yang, H. Wang, Facile assembled biochar-based nanocomposite with improved graphitization for efficient photocatalytic activity driven by visible light, Appl. Catal. B-Environ. 250 (2019) 78–88.

[34] B. Song, M. Chen, S. Ye, P. Xu, G. Zeng, J. Gong, J. Li, P. Zhang, W. Cao, Effects of multi-walled carbon nanotubes on metabolic function of the microbial community in riverine sediment contaminated with phenanthrene, Carbon 144 (2019) 1–7.

[35] D. Zhao, C.L. Dong, B. Wang, C. Chen, Y.C. Huang, Z. Diao, S. Li, L. Guo, S. Shen, Synergy of dopants and defects in graphitic carbon nitride with exceptionally modulated band structures for efficient photocatalytic oxygen evolution, Adv. Mater. 31 (2019) e1903545.

[36] Y. Yang, Z.T. Zeng, G.M. Zeng, D.L. Huang, R. Xiao, C. Zhang, C.Y. Zhou, W.P. Xiong, W.J. Wang, M. Cheng, W.J. Xue, H. Guo, X. Tang, D.H. He, Ti3C2 Mxene/porous g-C3N4 interfacial Schottky junction for boosting spatial charge separation in photocatalytic H2O2 production, Appl. Catal. B-Environ. 258 (2019) 11.

[37] K.C. Devarayapalli, S.V. Prabhakar Vattikuti, T.V. Madhukar Sreekanth, P. Chidanandha Nagajyothi, J. Shim, Pyrolysis-synthesized g-C_3N_4/Nb_2O_5 nanocomposite for enhanced photocatalytic activity under white LED light irradiation, ChemistrySelect 4 (2019) 13250–13258.

[38] W. Wang, Q. Niu, G. Zeng, C. Zhang, D. Huang, B. Shao, C. Zhou, Y. Yang, Y. Liu, H. Guo, W. Xiong, L. Lei, S. Liu, H. Yi, S. Chen, X. Tang, 1D porous tubular g-C3N4 capture black phosphorus quantum dots as 1D/0D metal-free photocatalysts for oxytetracycline hydrochloride degradation and hexavalent chromium reduction, Appl. Catal. B 273 (2020) 119051.

[39] Y.-J. Yuan, Z. Shen, S. Wu, Y. Su, L. Pei, Z. Ji, M. Ding, W. Bai, Y. Chen, Z.-T. Yu, Z. Zou, Liquid exfoliation of g-C3N4 nanosheets to construct 2D–2D MoS2/g-C3N4 photocatalyst for enhanced photocatalytic H2 production activity, Appl. Catal. B 246 (2019) 120–128.

[40] T.S. Natarajan, K.R. Thampi, R.J. Tayade, Visible light driven redox-mediator-free dual semiconductor photocatalytic systems for pollutant degradation and the ambiguity in applying Z-scheme concept, Appl. Catal. B 227 (2018) 296–311.

[41] Z. Zhang, L. Bai, Z. Li, Y. Qu, L. Jing, Review of strategies for the fabrication of heterojunctional nanocomposites as efficient visible-light catalysts by modulating excited electrons with appropriate thermodynamic energy, J. Mater. Chem. A 7 (2019) 10879–10897.

[42] Z. Wei, M. Liu, Z. Zhang, W. Yao, H. Tan, Y. Zhu, Efficient visible-light-driven selective oxygen reduction to hydrogen peroxide by oxygen-enriched graphitic carbon nitride polymers, Energy Environ. Sci. 11 (2018) 2581–2589.

[43] C. Lai, F. Huang, G. Zeng, D. Huang, L. Qin, M. Cheng, C. Zhang, B. Li, H. Yi, S. Liu, L. Li, L. Chen, Fabrication of novel magnetic MnFe2O4/bio-char composite and heterogeneous photo-Fenton degradation of tetracycline in near neutral pH, Chemosphere 224 (2019) 910–921.

[44] C. Zhou, C. Lai, P. Xu, G. Zeng, D. Huang, Z. Li, C. Zhang, M. Cheng, L. Hu, J. Wan, F. Chen, W. Xiong, R. Deng, Rational design of carbon-doped carbon Nitride/Bi12O17Cl2 composites: a promising candidate photocatalyst for boosting visible-light-driven photocatalytic degradation of tetracycline, ACS Sustain. Chem. Eng. 6 (2018) 6941–6949.

[45] H. Wang, Y. Wu, M. Feng, W. Tu, T. Xiao, T. Xiong, H. Ang, X. Yuan, J.W. Chew, Visible-light-driven removal of tetracycline antibiotics and reclamation of hydrogen energy from natural water matrices and wastewater by polymeric carbon nitride foam, Water Res. 144 (2018) 215–225.

[46] C. Lai, M. Wang, G. Zeng, Y. Liu, D. Huang, C. Zhang, R. Wang, P. Xu, M. Cheng,

C. Huang, Synthesis of surface molecular imprinted TiO_2/graphene photocatalyst and its highly efficient photocatalytic degradation of target pollutant under visible light irradiation, Appl. Surf. Sci. 390 (2016) 368–376.

[47] B. Li, C. Lai, G. Zeng, L. Qin, H. Yi, D. Huang, C. Zhou, X. Liu, M. Cheng, P. Xu, C. Zhang, F. Huang, S. Liu, Facile hydrothermal synthesis of Z-scheme Bi2Fe4O9/Bi2WO6 heterojunction photocatalyst with enhanced visible light photocatalytic activity, ACS Appl. Mater. Interfaces 10 (2018) 18824–18836.

[48] W. Wang, Z. Zeng, G. Zeng, C. Zhang, R. Xiao, C. Zhou, W. Xiong, Y. Yang, L. Lei, Y. Liu, D. Huang, M. Cheng, Y. Yang, Y. Fu, H. Luo, Y. Zhou, Sulfur doped carbon quantum dots loaded hollow tubular g-C3N4 as novel photocatalyst for destruction of Escherichia coli and tetracycline degradation under visible light, Chem. Eng. J. 378 (2019) 122132.

[49] H. Huang, K. Xiao, N. Tian, F. Dong, T. Zhang, X. Du, Y. Zhang, Template-free precursor-surface-etching route to porous, thin g-C3N4 nanosheets for enhancing photocatalytic reduction and oxidation activity, J. Mater. Chem. A 5 (2017) 17452–17463.

[50] H.W. Kim, M.B. Ross, N. Kornienko, L. Zhang, J. Guo, P. Yang, B.D. McCloskey, Efficient hydrogen peroxide generation using reduced graphene oxide-based oxygen reduction electrocatalysts, Nat. Catal. 1 (2018) 282–290.

[51] Z. Lu, G. Chen, S. Siahrostami, Z. Chen, K. Liu, J. Xie, L. Liao, T. Wu, D. Lin, Y. Liu, T.F. Jaramillo, J.K. Nørskov, Y. Cui, High-efficiency oxygen reduction to hydrogen peroxide catalysed by oxidized carbon materials, Nat. Catal. 1 (2018) 156–162.

[52] A. Kaur, S.K. Kansal, Bi2WO6 nanocuboids: an efficient visible light active photocatalyst for the degradation of levofloxacin drug in aqueous phase, Chem. Eng. J. 302 (2016) 194–203.

[53] H. Yi, M. Jiang, D. Huang, G. Zeng, C. Lai, L. Qin, C. Zhou, B. Li, X. Liu, M. Cheng, W. Xue, P. Xu, C. Zhang, Advanced photocatalytic Fenton-like process over biomimetic hemin-Bi_2WO_6 with enhanced pH, J. Taiwan Inst. Chem. Eng. 93 (2018) 184–192.

[54] X. Cao, Z. Chen, R. Lin, W.-C. Cheong, S. Liu, J. Zhang, Q. Peng, C. Chen, T. Han, X. Tong, Y. Wang, R. Shen, W. Zhu, D. Wang, Y. Li, A photochromic composite with enhanced carrier separation for the photocatalytic activation of benzylic C-H bonds in toluene, Nat. Catal. 1 (2018) 704–710.

[55] S. Ye, G. Zeng, H. Wu, C. Zhang, J. Liang, J. Dai, Z. Liu, W. Xiong, J. Wan, P. Xu, M. Cheng, Co-occurrence and interactions of pollutants, and their impacts on soil remediation – a review, Crit. Rev. Environ. Sci. Technol. 47 (2017) 1528–1553.

[56] L. Qin, H. Yi, G. Zeng, C. Lai, D. Huang, P. Xu, Y. Fu, J. He, B. Li, C. Zhang, M. Cheng, H. Wang, X. Liu, Hierarchical porous carbon material restricted Au catalyst for highly catalytic reduction of nitroaromatics, J. Hazard. Mater. 380 (2019) 120864–120864.

[57] B. Li, C. Lai, L. Qin, C. Chu, M. Zhang, S. Liu, X. Liu, H. Yi, J. He, L. Li, M. Li, L. Chen, Anchoring single-unit-cell defect-rich bismuth molybdate layers on ultrathin carbon nitride nanosheet with boosted charge transfer for efficient photocatalytic ciprofloxacin degradation, J. Colloid Interface Sci. 560 (2020) 701–713.

[58] L. Qin, Z. Zeng, G. Zeng, C. Lai, A. Duan, R. Xiao, D. Huang, Y. Fu, H. Yi, B. Li, X. Liu, S. Liu, M. Zhang, D. Jiang, Cooperative catalytic performance of bimetallic Ni-Au nanocatalyst for highly efficient hydrogenation of nitroaromatics and corresponding mechanism insight, Appl. Catal. B 259 (2019) 118035.

[59] L. Yue, S. Wang, G. Shan, W. Wu, L. Qiang, L. Zhu, Novel MWNTs–Bi2WO6 composites with enhanced simulated solar photoactivity toward adsorbed and free tetracycline in water, Appl. Catal. B 176–177 (2015) 11–19.

[60] H. Yi, M. Yan, D. Huang, G. Zeng, C. Lai, M. Li, X. Huo, L. Qin, S. Liu, X. Liu, B. Li, H. Wang, M. Shen, Y. Fu, X. Guo, Synergistic effect of artificial enzyme and 2D nano-structured Bi2WO6 for eco-friendly and efficient biomimetic photocatalysis, Appl. Catal. B 250 (2019) 52–62.

[61] H. Li, H. Shang, Y. Li, X. Cao, Z. Yang, Z. Ai, L. Zhang, Interfacial charging-decharging strategy for efficient and selective aerobic NO oxidation on oxygen vacancy, Environ. Sci. Technol. 53 (2019) 6964–6971.

[62] Y. Yang, Z. Zeng, C. Zhang, D. Huang, G. Zeng, R. Xiao, C. Lai, C. Zhou, H. Guo, W. Xue, M. Cheng, W. Wang, J. Wang, Construction of iodine vacancy-rich BiOI/Ag@AgI Z-scheme heterojunction photocatalysts for visible-light-driven tetracycline degradation: transformation pathways and mechanism insight, Chem. Eng. J. 349 (2018) 808–821.

[63] M. Li, C. Lai, H. Yi, D. Huang, L. Qin, X. Liu, B. Li, S. Liu, M. Zhang, Y. Fu, L. Li, J. He, Y. Zhang, L. Chen, Multiple charge-carrier transfer channels of Z-scheme bismuth tungstate-based photocatalyst for tetracycline degradation: transformation pathways and mechanism, J. Colloid Interface Sci. 555 (2019) 770–782.

[64] Z.P. Nie, D.K. Ma, G.Y. Fang, W. Chen, S.M. Huang, Concave Bi2WO6 nanoplates with oxygen vacancies achieving enhanced electrocatalytic oxygen evolution in near-neutral water, J. Mater. Chem. A 4 (2016) 2438–2444.

[65] C. Lai, M. Zhang, B. Li, D. Huang, G. Zeng, L. Qin, X. Liu, H. Yi, M. Cheng, L. Li, Z. Chen, L. Chen, Fabrication of CuS/BiVO4 (0 4 0) binary heterojunction photocatalysts with enhanced photocatalytic activity for Ciprofloxacin degradation and mechanism insight, Chem. Eng. J. 358 (2019) 891–902.

[66] Y. Fu, L. Qin, D. Huang, G. Zeng, C. Lai, B. Li, J. He, H. Yi, M. Zhang, M. Cheng, X. Wen, Chitosan functionalized activated coke for Au nanoparticles anchoring: Green synthesis and catalytic activities in hydrogenation of nitrophenols and azo dyes, Appl. Catal. B-Environ. 255 (2019).

[67] L. Ge, J. Chen, S. Zhang, X. Cai, Z. Wang, C. Wang, Photodegradation of fluoroquinolone antibiotic gatifloxacin in aqueous solutions, Chin. Sci. Bull. 55 (2010) 1495–1500.

[68] S. Luo, J. Ke, M. Yuan, Q. Zhang, P. Xie, L. Deng, S. Wang, $CuInS_2$ quantum dots embedded in Bi_2WO_6 nanoflowers for enhanced visible light photocatalytic removal of contaminants, Appl. Catal. B: Environ. 221 (2018) 215–222.

[69] Q. Huo, X. Qi, J. Li, G. Liu, Y. Ning, X. Zhang, B. Zhang, Y. Fu, S. Liu, Preparation of a direct Z-scheme α-Fe2O3/MIL-101(Cr) hybrid for degradation of carbamazepine under visible light irradiation, Appl. Catal. B 255 (2019) 117751.

[70] K.C. Devarayapalli, S.V.P. Vattikuti, T.V.M. Sreekanth, K.S. Yoo, P.C. Nagajyothi, J. Shim, Hydrogen production and photocatalytic activity of g-C3N4/Co-MOF (ZIF-67) nanocomposite under visible light irradiation, Appl. Organomet. Chem. 34 (2020) e5376.

[71] W. Jiang, X. Zong, L. An, S. Hua, X. Miao, S. Luan, Y. Wen, F.F. Tao, Z. Sun, Consciously constructing heterojunction or direct Z-scheme photocatalysts by regulating electron flow direction, ACS Catal. 8 (2018) 2209–2217.